

# Assessing lidar-assisted feedforward and multivariable feedback controls for large floating wind turbines

Feng Guo<sup>1</sup> and David Schlipf<sup>1</sup>

<sup>1</sup>Wind Energy Technology Institute, Flensburg University of Applied Sciences, Kanzleistraße 91-93, 24943 Flensburg, Germany

**Correspondence:** Feng Guo (feng.guo@hs-flensburg.de)

**Abstract.** We assess the performance of two control strategies on the IEA 15 MW reference floating wind turbine through OpenFAST simulations. The multivariable feedback controller tuned by the toolbox of the Reference Open Source Controller (ROSCO) is considered as a benchmark for comparison. We then tune the feedback gains for the multi-variable controller, considering two cases: with and without lidar-assisted feedforward control. The tuning process is performed using OpenFAST  
5 simulations, considering realistic offshore turbulence spectral parameters. We reveal that optimally tuned controllers are robust to changes in turbulence parameters caused by atmospheric stability variations. Compared to the baseline multivariable controller, the one with optimal tuning significantly reduced the tower damage equivalent load, which results in a lifetime extension of 19.2 years. With the assistance of feedforward control provided by a typical four-beam lidar, compared with the optimally tuned MVFB control, the lifetime of the tower can be extended by 5.1 years.

## 10 1 Introduction

In recent years, more and more floating wind projects have emerged, such as Hywind Scotland, WindFloat Atlantic (Portugal), Kincardine (Scotland), Hywind Tampen (Norway), Sanxia Yinling Hao (China), and Fuyao (China). One thing in common is that all these projects use floating offshore wind turbines (FOWTs) with rotor diameters above 150 m. Similar to the bottom-fixed wind turbine, using large wind turbines with higher capacity is the key driver to reduce the levelized cost of energy for  
15 floating wind projects (CATAPULT, 2021).

The floating wind turbines have extra degrees of freedom (DOF) compared to a bottom-fixed turbine. Both the aerodynamic forces from the wind and the hydrodynamic forces from the wave can excite the structural motions of the FOWT, resulting in fatigue loads. Under the same wind speed conditions, when the rotor radius increases, At the same wind speed, the rotor swept-area of the turbine increases quadratically when the rotor radius increases, and the aerodynamic thrust on the rotor increases  
20 accordingly. As the rotor becomes larger, the inertia of the FOWT system also increases, leading to a smaller natural frequency of most structural motions (Wu and Kim, 2021). Typically, the platform of FOWT is designed to have a natural frequency of the platform pitch motion outside and lower than the range where the variation of wave height has most of the energy. However, there are more large-scale coherent variations of turbulent wind at lower frequency ranges (Knight and Obhrai, 2019; Bachynski and Eliassen, 2019; Nybø et al., 2020; Guo et al., 2023; Rivera-Arreba et al., 2022); therefore, the most important

25 motions such as platform surge and pitch are dominated by the turbulent wind for large FOWTs. The platform pitch fore-aft motion causes changes in the relative wind speed and imposes the tower bottom bending moment. In addition, the platform surge causes tension changes in the mooring system (Somoano et al., 2021). Thus, the aerodynamic-driven pitch and surge motions of FOWTs are significant for mechanical loads, and they lead to a challenging control system design (Lemmer, 2018; Lemmer et al., 2020).

30 The lidar system can remotely measure the line-of-sight (LOS) wind speed, which is the wind velocity vector projected onto the laser beam direction. A lidar-assisted control (LAC) system processes the LOS speed measurements and provides a preview of the incoming turbulent wind, namely the lidar-estimated rotor effective wind speed (REWS) for feedforward control of wind turbines. Currently, lidar-assisted collective pitch feedforward (LACPF) control has been applied commercially for bottom-fixed turbines, and it has been revealed by several authors to be able to improve rotor speed regulation and reduce  
35 structural loads, e.g., by Bossanyi et al. (2014); Schlipf (2015); Lio et al. (2022); Meng et al. (2022); Guo et al. (2023). In terms of applying LACPF to floating turbines, Schlipf et al. (2015) found better rotor speed regulations and lower structural loads for a floating spar-type 5.0MW turbine. In the studies above, the LAC system is designed to compensate for aerodynamic torque changes caused by wind and therefore aims to improve rotor speed regulation. On the other hand, Schlipf et al. (2020) designed a lidar-assisted pitch control algorithm that offsets the aerodynamic thrust force variation owing to the turbulent wind  
40 and utilizes the generator torque to compensate for the aerodynamic torque change resulting from blade pitch actions. This algorithm improves rotor speed regulation and reduces tower and blade fatigue loads for the DTU 10 MW Triple Spar floating turbine (Bredmose et al., 2017), but it requires a high level of variability in the generator torque.

In addition, the multivariable feedback (MVFB) controller is also considered beneficial for stabilizing the fore-aft pitch motion and reducing structural loads on FOWTs. Compared with the conventional single-variable (generator speed) feedback  
45 controller, variables associated with fore-aft motion, such as tower top position (van der Veen et al., 2012), velocity (Abbas et al., 2022), or platform pitch angle (Fleming et al., 2019), are also fed back in a multivariable feedback controller. These signals provide additional blade pitch signals through a feedback loop that, if properly adjusted, can increase the damping of the floating platform.

Currently, there is a lot of literature available on optimizing the parameters of floating wind turbine controllers. Many of these  
50 optimizations aim for controller parameters that minimize turbine fatigue loads while staying within safe operating boundaries. For example, in the studies by Sandner et al. (2014), Lemmer et al. (2017) and Lemmer et al. (2020), the reduced-order model is applied to find optimized gains for the conventional Proportional-Integral (PI) controller. There are also studies that use nonlinear aeroelastic simulations to find optimized parameters for a multi-variable feedback controller, such as the study by Zalkind et al. (2022). In terms of re-tuning and optimizing feedback gains with LAC, Schlipf et al. (2018) used a sequential  
55 approach to improving the benefits of LAC for onshore turbines, considering a reduced-order nonlinear turbine model.

In this work, we perform optimization of feedback gains for a MVFB controller and a LACPF+MVFB controller using non-linear OpenFAST simulations. After optimizing controller parameters, the controller's performance is assessed using realistic offshore turbulence characteristics and considering the variability of turbulence parameters related to atmospheric stability conditions. A nomenclature of symbols used in this paper is provided in Table 1.

**Table 1.** Nomenclature.

Symbols	Definitions	Units
$U_{10\min}$	mean wind speed at 10 m above sea level	$\text{m s}^{-1}$
$U_{\text{hub}}$	turbine hub-height mean wind speed	$\text{m s}^{-1}$
$U_{\text{Ref}}$	mean wind speed for turbulence convection	$\text{m s}^{-1}$
$T_{\text{p}}$	peak wave spectral period	s
$H_{\text{s}}$	spectral significant wave height	m
$P_{U_{\text{hub}}}$	probability distribution of hub-height mean wind and wave conditions	-
$L$	turbulence length scale	m
$\Gamma$	turbulence anisotropy	-
$\alpha\varepsilon^{2/3}$	energy level constant	$\text{m}^{4/3} \text{s}^{-2}$
$\zeta$	atmosphere stability parameter	-
$f$	frequency	Hz
$\gamma$	eddy lifetime parameter	s
$P_{\text{sta}}$	probability distributions of atmospheric stability	-
$\Omega_{\text{g}}$	generator speed	$\text{rad s}^{-1}$
$\dot{\beta}_{\text{p}}$	platform pitch rate (angular speed)	$\text{rad s}^{-1}$
$k_{\text{p, float}}$	floating feedback gain	s
$\theta_{\text{float}}$	blade pitch command by the floating feedback loop	rad
$\theta_{\text{e, RFB}}$	blade pitch command by the reference PI control	rad
$k_{\text{p}}$	proportional gain	s
$T_{\text{I}}$	integral time constant	s
$v_{\text{los, mc}}$	motion-compensated lidar LOS speed measurement	$\text{m s}^{-1}$
$v_{\text{los}}$	raw lidar LOS speed measurement	$\text{m s}^{-1}$
$\mathbf{v}_{\text{lidar}}$	lidar translational velocity	$\text{m s}^{-1}$
$\mathbf{n}$	unit vector aligns with the lidar beam direction	-
$u_{\text{LL, est}}$	lidar-estimated REWS	$\text{m s}^{-1}$
$\dot{\theta}_{\text{FF}}$	feedforward blade pitch rate	$\text{rad s}^{-1}$
$G_{\text{RL}}$	transfer function gain	-
$S_{\text{RL}}$	cross-spectrum between lidar-estimated and rotor-based REWSs	$\text{m}^2 \text{s}^{-2} \text{Hz}^{-1}$
$S_{\text{LL}}$	auto-spectrum of lidar-estimated REWS	$\text{m}^2 \text{s}^{-2} \text{Hz}^{-1}$
$f_{\text{cutoff}}$	filter cutoff frequency	Hz
$T_{\text{buffer}}$	buffer time of the feedforward controller	s
$T_{\text{lead}}$	leading preview time or time required for turbulence convection	s
$T_{\text{filter}}$	time lag caused by filtering	s
$T_{\text{pitch}}$	time lag of the blade pitch actuator	s
$T_{\text{lidar}}$	lidar full-scan time	s
$\Delta x$	distance between the lidar-measured plane and the rotor position	m
$U_{\text{Ref}}$	mean wind speed of turbulence convection	$\text{m s}^{-1}$
$\beta_{\text{oa}}$	lidar beam opening angle	deg
$A_{\text{eq}}$	equivalent load amplitude	load specific
$m$	Wöhler exponent	-

60 The rest of this paper is structured as follows: Section 2 provides some background about the floating turbine model, environment conditions, and lidar system; Section 3 illustrates the design of MVFB and LACPF+MVFB controllers; Section 4 presents the tuning of the feedback gains; Section 5 assesses the optimally tuned controllers; and lastly, Section 6 concludes this paper and proposes further work.

## 2 Background

65 This section provides background about the FOWT, wind and wave conditions, and the lidar system.

### 2.1 Floating wind turbine model

The IEA 15MW semi-submersible floating wind turbine, developed collaboratively by NREL, DTU, and UMaine (Gaertner et al. 2020), is considered in this work. This reference floating turbine has a rotor diameter of 240 m and a hub height of 150 m. It uses a steel semi-submersible floating structure designed by UMaine (Allen et al., 2020). The turbine model has been  
70 made openly available from the IEA Wind Task 37 GitHub repository. The latest FOWT model built for OpenFAST version 3.0 is used in this research<sup>1</sup>. A sketch of the reference turbine and the inertial coordinate system is shown in Figure 1. The longitudinal direction (along the  $x$  axis) is considered the mean wind direction. The directions of platform motions in this work follow the right-hand rule according to the inertial coordinate system.

### 2.2 Wind and wave

75 To assess the controller's performance using realistic offshore environment conditions, we consider the wind and wave joint distribution, according to the study by Bachynski and Eliassen (2019). The data was selected by Bachynski and Eliassen (2019) according to the analysis of hindcast data by Li et al. (2013). The selected site corresponds to site No. 14, which is located in the North Sea and is 30 km away from the western Norwegian coast. The water depth of this site is 202 m which is close to the design depth (200 m) of the FOWT model (Allen et al., 2020). This site data is also used by Bachynski and Eliassen (2019)  
80 to analyze the fatigue loads of FOWT. According to Li et al. (2013), the probability distribution of the one-hour mean wind speed at 10 m above sea level ( $U_{10m}$ ) follows a Weibull distribution with shape and scale parameters equivalent to 2.02 and 9.41, respectively. We use these Weibull parameters and assume a power log shear exponent of 0.14, as specified by the IEC 61400-1 (2019) standard, to obtain the probability distribution ( $P_{U_{hub}}$ ) of turbine hub-height mean wind speed ( $U_{hub}$ ), which is summarized in Table 2. The second and third rows correspond to the peak wave spectral period  $T_p$  and the spectral significant  
85 wave height  $H_s$ , respectively. For a specific mean wind speed, these are the most representative conditions (Bachynski and Eliassen, 2019). The stochastic irregular waves are generated using these two wave parameters, according to the JONSWAP spectra (IEC 61400-3, 2009).

The extended four-dimensional (4D) Mann turbulence model (Guo et al., 2022a) is considered to model turbulent wind fields, which considers turbulence evolution. The 4D Mann model assumes stationary stochastic turbulence fields, meaning

---

<sup>1</sup> Accessible: <https://github.com/IEAWindTask37/IEA-15-240-RWT/tree/ed7e726062a1355fd0355cdb4fba739fb682ff9e>.

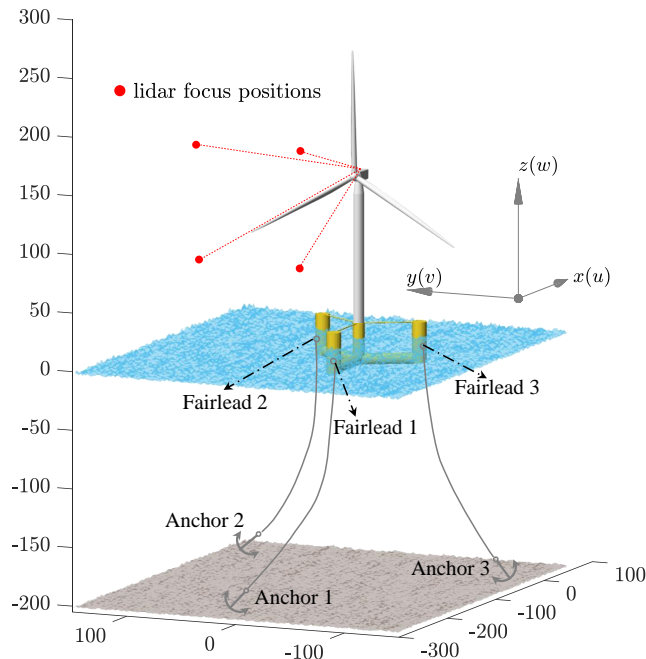


**Figure 1.** A sketch of the investigated IEA 15MW reference turbine equipped with a four-beam nacelle lidar system and a UMaine semi-submersible floating platform, drawn using the CAD data provided by the IEA Wind Task 37 GitHub repository. The coordinate system follows the right-hand rule (with a unit in m) and is applicable to the full paper. Note that the positions of the anchors are not true values due to the limitations of the figure frame.

**Table 2.** Distributions of mean wind and wave characteristics used for aeroelastic simulations.

$U_{\text{hub}}$ [ $\text{m s}^{-1}$ ]	4.0	6.0	8.0	10.0	12.0	14.0	16.0	18.0	20.0	22.0	24.0
$U_{10\text{m}}$ [ $\text{m s}^{-1}$ ]	2.7	4.1	5.5	6.8	8.2	9.6	11.0	12.3	13.7	15.1	16.4
$H_s$ [m]	1.5	1.7	1.8	2.0	2.3	2.6	3.0	3.4	3.8	4.2	4.7
$T_p$ [s]	9.3	9.5	9.6	9.8	10.0	10.3	10.5	10.7	11.0	11.3	11.6
$P_{U_{\text{hub}}}$ [-]	0.056	0.076	0.088	0.092	0.087	0.077	0.064	0.050	0.037	0.026	0.017

90 that the statistics of both upstream and downstream turbulence fields follow the statistics described by the Mann spectral tensor (Mann, 1994). The main reason to use the extended Mann model for the assessment in this work is that the lidar system needs to measure at a far distance in front of the rotor for LAC (as discussed in Section 3.2.2); therefore, it is not realistic to assume Taylor's frozen hypothesis (Taylor, 1938) with which the turbulence structures are assumed to be unchanged when propagating from upstream to downstream positions. More details about the 4D Mann turbulence model can be found in the work by Guo  
 95 et al. (2022a).

As studied by several authors (de Maré and Mann, 2014; Cheynet et al., 2017; Peña, 2019; Putri et al., 2022), the turbulence spectral parameters can vary from the values specified in the IEC 61400-1 (2019) standard, and they change with atmospheric

stability. Thus, we fit the Mann turbulence parameters: length scale  $L$  and anisotropy parameter  $\Gamma$ , according to the spectral analysis results of offshore FINO1 site<sup>2</sup> data performed by Cheynet et al. (2018). The fitting process relies on minimizing the root mean square error between the FINO1 data- and the Mann model-based spectra (see Guo et al. (2023) for the detailed fitting process). Another concern with considering the offshore turbulence spectral parameter is that these parameters are related to lidar wind preview for turbine control (Guo et al., 2023), and the platform motion is primarily linked to the turbulence length scale for a certain turbulence intensity (TI) level. With a larger length scale, there are larger coherent turbulent eddies, and they have greater potential to excite the low-frequency platform modes more severely, resulting in higher structural loads (Bachynski and Eliassen, 2019). The three most frequent stability classes from the study by Cheynet et al. (2018) are considered in this paper. These stability classes are characterized by a stability parameter  $\zeta$  related to the reference height and Obukhov length (Obukhov, 1971). Table 3 summarizes the fitted Mann parameters and the probability distribution (Cheynet et al., 2018) of the three stability classes in each mean wind speed range. In terms of the energy level constant  $\alpha\varepsilon^{2/3}$ , it is scaled to follow a TI level corresponding to the Class C turbine specified by IEC 61400-1 (2019). The equations provided by the offshore standard IEC 61400-3 (2009) are used to calculate the standard deviations of the wind velocity components. Figure 2 shows the fitted spectra of longitudinal velocity components, where the fitted spectra generally agree with the estimated spectra from the FINO1 measurement site. Note that we only consider the frequency range with  $0.001 < f < 2$  Hz in the fitting process and ignore the turbulence fluctuations of lower frequencies because they are less significant for the turbine motions and loads.

In the 4D Mann turbulence model, there is an additional parameter that defines the severity of turbulence evolution, namely, the eddy lifetime  $\gamma$ . Thus far, there is limited literature that studies the distribution of this parameter under different atmospheric stability classes in an offshore environment. We chose this parameter according to the study by Guo et al. (2023), which is a summary of several works that studied turbulence evolution by onshore measurements (coastal, flat terrain). In this work, the eddy lifetimes of unstable, neutral, and stable atmospheric conditions used by Guo et al. (2023) are used for stability 1, 2, and 3, respectively, because of the high similarity of the stability parameter  $\zeta$ .

To perform aeroelastic simulations using OpenFAST, we generate turbulence boxes using the 4D Mann turbulence generator<sup>3</sup>. Each 4D turbulence box has dimensions of  $2048 \times 2 \times 64 \times 64$  grid points, corresponding to the time and the  $x$ ,  $y$  and  $z$  directions. The lengths in the  $y$  and  $z$  directions are both 288 m. Note that the original turbulence boxes have a dimension of 128 grid points in both the  $y$  and  $z$  directions, but they are cropped to avoid the periodicity inherited from the three-dimensional inverse Fourier transform (Mann, 1998). The two  $y$ - $z$  planes in the  $x$  direction are used for simulating lidar measurements and turbine aerodynamics, respectively. Since the total number of time steps is 2048, we chose a time step of 0.293 s for the turbulence field, which leads to a total time length of 600 s. Note that the simulation time length of 600 s is selected according to the IEC 61400-1 (2019) standard. Similarly, the irregular waves are generated using the same time step and length as the turbulent wind. Both wind fields and waves are assumed to be periodic in time.

<sup>2</sup>FINO1 is an offshore research platform located at North Sea in a water depth close to 30m: <https://www.fino1.de/de/standort.html>

<sup>3</sup>The 4D Mann turbulence generator is accessible from <https://github.com/MSCA-LIKE/4D-Mann-Turbulence-Generator>

**Table 3.** The Mann model parameters under different atmospheric stability conditions fitted using the spectral analysis of FINO1 data by Cheynet et al. (2018) and their probability distributions  $P_{sta}$  [-] at different mean wind speeds. The atmospheric stability is classified by the stability parameter  $\zeta$ . The energy level constant  $\alpha\varepsilon^{2/3}$  [ $\text{m}^{4/3} \text{s}^{-2}$ ] is scaled to follow a TI level corresponding to the Class C turbine specified by IEC 61400-1 (2019).

$\zeta \in$	Stability 1 [-0.3,-0.1)		Stability 2 [-0.1,0.1)		Stability3 [0.1,0.3)	
$L$ [m]	139		73		26	
$\Gamma$ [-]	2.3		2.6		2.8	
$\gamma$ [s]	600		400		200	
$U_{hub}$	$P_{sta}$	$\alpha\varepsilon^{2/3}$	$P_{sta}$	$\alpha\varepsilon^{2/3}$	$P_{sta}$	$\alpha\varepsilon^{2/3}$
4.0	0.75	0.02	0.125	0.03	0.125	0.05
6.0	0.70	0.03	0.20	0.04	0.10	0.07
8.0	0.55	0.04	0.20	0.05	0.25	0.09
10.0	0.30	0.05	0.50	0.06	0.20	0.12
12.0	0.20	0.06	0.625	0.08	0.175	0.15
14.0	0.10	0.07	0.75	0.10	0.15	0.19
16.0	0.05	0.09	0.80	0.12	0.15	0.23
18.0	0.03	0.11	0.87	0.15	0.10	0.28
20.0	0.02	0.13	0.93	0.18	0.05	0.33
22.0	0.00	0.16	1.00	0.21	0.00	0.39
24.0	0.00	0.18	1.00	0.25	0.00	0.46

### 2.3 Lidar system

- 130 We consider a typical four-beam commercially available pulsed lidar configuration for this study. In practice, the pulsed lidar system is able to provide measurements from different range gates along the laser direction. We only consider one measurement range gate in this work. As a result, this lidar system only relies on a simple lidar data processing algorithm for feedforward control. Before implementing the LAC, the lidar measurement trajectory optimization is presented in Section 3.2.2, which aims to find optimal opening angles of laser beams and upstream focused distance.
- 135 To simulate a realistic lidar system in the OpenFAST environment, we use the lidar module-integrated OpenFAST version 3.0, in which a realistic lidar simulation module is updated by Guo et al. (2022b). The updated lidar module considers realistic lidar measurement properties, including the probe volume averaging effect along the LOS direction, the contribution of the nacelle movement to the LOS measurement, laser beam blockage caused by turbine blade passing, the turbulence evolution, and the adjustable measurement availability. In some special weather patterns, such as extreme fog, heavy rain, and an extremely
- 140 clear sky, the lidar system does not always provide reliable measurements due to a low carrier-to-noise ratio caused by low

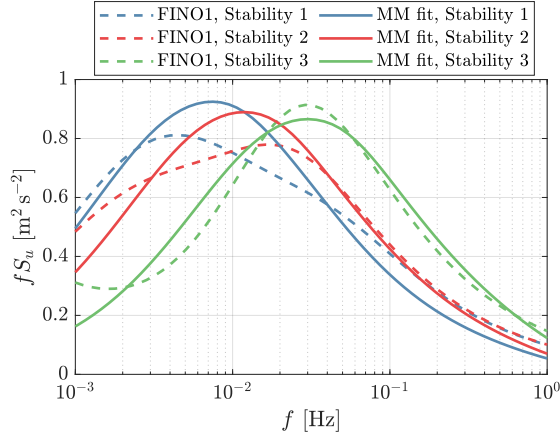


**Figure 2.** The estimated spectra using FINO1 measurement data by Cheynet et al. (2018) and the fitted Mann model-based spectra (indicated as MM fit in the legend). The spectra shown here are calculated assuming a mean wind speed of  $16 \text{ m s}^{-1}$ . The spectra are normalized to have the standard deviations correspond to  $\text{TI}=12\%$ .

backscattering. However, in this work, we ignore the low availability caused by special weather conditions and only consider the remaining three characteristics in the simulations.

### 3 Controller design

In this section, we first describe the MVFB controller and then discuss the design of the lidar-assisted controller.

#### 145 3.1 Multivariable feedback controller

Apart from the generator speed  $\Omega_g$ , the MVFB control additionally feeds back the platform pitch rate  $\dot{\beta}_p$ , or rotational speed, in another word, as shown in Figure 3. In this work, we have modified the lidar-integrated OpenFAST 3.0 and ROSCO version 2.6.0 (NREL, 2021) to be able to use the platform pitch rate for the floating feedback loop. In the floating feedback loop, the pitch angle  $\theta_{\text{float}}$  is simply determined by

$$150 \quad \theta_{\text{float}} = k_{p,\text{float}} \dot{\beta}_{p,\text{BPF}}, \quad (1)$$

where  $\dot{\beta}_{p,\text{BPF}}$  is the band-pass filtered platform pitch rate and  $k_{p,\text{float}}$  is a constant gain. A detailed description and the source code of the NREL ROSCO controller can be found in the works by Abbas et al. (2022); NREL (2021).

Depending on the sign of floating feedback gain  $k_{p,\text{float}}$ , the floating feedback loop can compensate for the relative wind speed change caused by platform motion or provide damping effects to the platform pitch motion. Based on the coordinate  
 155 system used in this work, a positive gain is selected that aims for platform damping. For example, a positive platform pitch



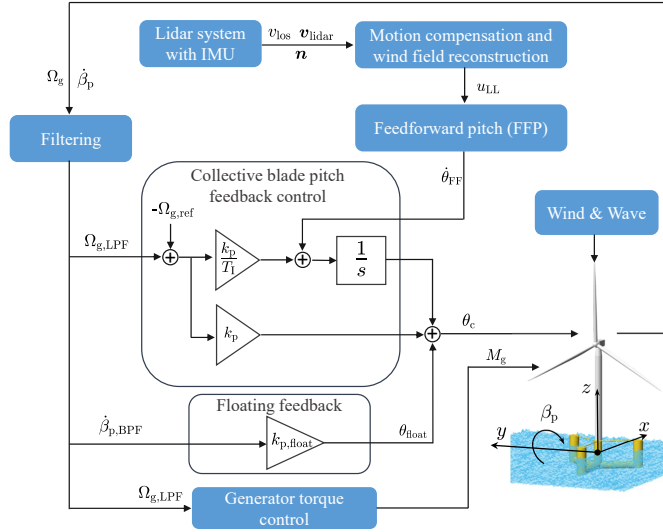


**Figure 3.** The overall control diagram for a floating wind turbine. Note that the real-time pitch angle ( $\theta$ ) signal is also used in the generator torque control and collective blade pitch feedback control modules for controller scheduling, but the lines are omitted.

motion means that the rotor is pushed backwards, which leads to an increase in blade pitch and eventually a decrease in aerodynamic thrust on the rotor.

As for the regular collective blade pitch feedback loop, we use the PI controller already developed in ROSCO, i.e.,

$$\theta_{c,\text{RFB}} = k_p \Delta\Omega + \frac{1}{s} \left( \frac{k_p}{T_I} \Delta\Omega \right), \quad (2)$$

160 with  $\Delta\Omega = \Omega_{g,\text{LPF}} - \Omega_{g,\text{ref}}$ . Here,  $\theta_{c,\text{RFB}}$  is the pitch command of the reference feedback-only control (without LAC),  $k_p$  is the proportional gain,  $T_I$  is the integral time constant,  $\Omega_{g,\text{ref}}$  is the speed control reference, and  $\Omega_{g,\text{LPF}}$  is the low-pass filtered generator speed.

Figure 4 shows the response of the IEA 15MW floating turbine to an extreme operating gust (EOG) defined by the IEC 61400-1 (2019) standard. Here, no wave disturbance is considered in order to emphasize the response to wind disturbance.  
 165 The openloop results mean that both the blade pitch angles generator torque are kept as constant (steady state value). It can be seen that the open loop system is stable after the EOG. However, with the baseline single-variable (generator speed) feedback control, the system is not stable due to the famous “negative damping” problem of floating turbines (Jonkman, 2008; Ward et al., 2019). The system becomes stable again by introducing the floating feedback loop in the MVFB controller.

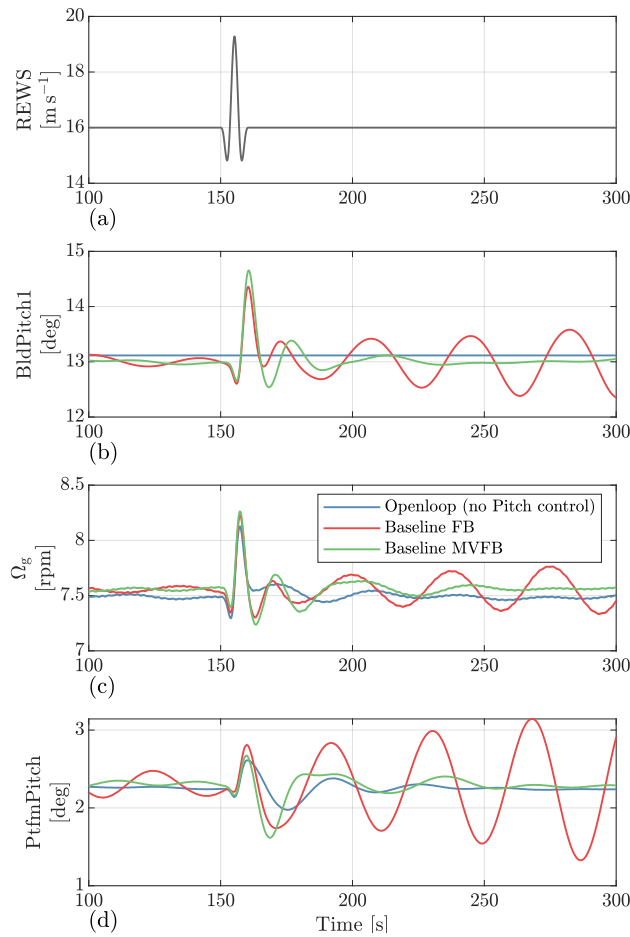


**Figure 4.** Time series of the OpenFAST simulations response to an extreme operating gust defined by the IEC 61400-1 (2019) standard. Baseline FB: single-variable (generator speed) feedback controller.

## 3.2 Lidar-assisted controller

### 170 3.2.1 Controller implementation

The LAC control in this work is designed for feedforward rotor speed regulation, mainly based on the work by Schlipf (2015). An open-source LAC implementation for onshore turbines has been developed by Guo et al. (2023). In this open-source LAC framework, a wrapper DLL calls first a lidar data processing (LDP) module, then a feedforward pitch (FFP) module, and lastly the ROSCO module. All these modules are written following the Bladed-style DLL data exchange interface (DNV-GL, 2016).

175 Compared to the onshore version of LAC, there are only two updates made for the LAC of floating turbines; therefore, we only

point out the differences in this work. For a more detailed description of LAC, please see the work by Guo et al. (2023); Schlipf (2015).

180 First, because the lidar LOS measurements are deteriorated by the nacelle motion and the motion is much more significant in the coupled-frequency ranges for floating turbines, the LOS measurement needs to be motion compensated (Schlipf et al., 2020). For onshore turbines, the nacelle motion is mainly caused by excitation of the tower's natural frequency, which lies in the frequency range above the cutoff frequency of the low-pass filter implemented in LAC. The amplitudes of tower top motions in the onshore cases are smaller than those of the floating cases; therefore, it may not be necessary to have a compensation algorithm. Differently, the natural frequencies of platform modes of floating turbines are in the low-frequency range, and they are not necessarily or completely filtered out by a standard filter design of LAC. If not compensated, the contribution of nacelle 185 motions becomes unnecessary pitch actuation in LAC and can result in undesired control behavior. Thus, we implement a compensation algorithm assuming a perfect inertial measurement unit (IMU), i.e.,

$$v_{\text{los,mc}} = v_{\text{los}} + \mathbf{v}_{\text{lidar}} \cdot \mathbf{n}. \quad (3)$$

Here,  $v_{\text{los}}$  is the LOS measurement by the lidar system,  $\mathbf{v}_{\text{lidar}}$  is the lidar translational velocity vector provided by the IMU,  $\mathbf{n} = (\cos \beta \cos \phi, \cos \beta \sin \phi, \sin \beta)$  is a unit vector aligned with the lidar beam direction, and  $v_{\text{los,mc}}$  is the LOS speed after 190 motion compensation. The unit vector  $\mathbf{n}$  can be simply calculated after knowing the azimuth angle  $\phi$  and elevation angle  $\beta$  of the lidar beam. We assume the positive  $x$  axis has zero azimuth and the positive  $z$  axis has  $90^\circ$  elevation. After motion compensation, the identical wind field reconstruction algorithm used by Guo et al. (2023) is applied in this work to obtain the lidar-estimated REWS  $u_{\text{LL,est}}$ .

Second, in the previous FFP module by Guo et al. (2023), only a low-pass filter was applied to the lidar-estimated REWS. 195 In this work, a notch filter is additionally introduced in the FFP module for the LAC of floating turbines. The main reason for the notch filter is to avoid conflicting with the floater damping control in the MVFB control. The floater damping is tuned to add a damping effect to the floater's fore-aft pitch motion by changing rotor thrust force, but the LAC aims to compensate for the change in aerodynamic torque. In the above-rated operation of typical turbine rotors, when the blade pitch is adjusted, both aerodynamic torque and rotor thrust increase or decrease together, so that only one control objective can be achieved. 200 Therefore, the notch filter is designed to have a cut-off frequency of 0.029 Hz, which is the natural frequency of the floating pitch motion. After low-pass and notch filtering the lidar-estimated REWS, the FFP module sends a blade pitch rate signal to the integrator of the collective pitch controller, as shown in Figure 3. Thus, the overall pitch command of the lidar-assisted feedforward multivariable feedback controller becomes

$$\theta_c = k_p \Delta \Omega + \frac{1}{s} \left( \frac{k_p}{T_I} \Delta \Omega + \dot{\theta}_{\text{FF}} \right) + k_{p,\text{float}} \dot{\beta}_{p,\text{BPF}}, \quad (4)$$

205 where  $s$  is the complex frequency.

### 3.2.2 Lidar Trajectory optimization

Due to several inherent characteristics, such as the misalignment to the longitudinal direction, turbulence evolution, and non-continuously available measurement, the lidar system does not provide a perfect estimation of the REWS (Guo et al., 2022a).

However, with a reasonable lidar data processing algorithm, it is able to provide a REWS that well-estimates the low-frequency variation of the actual effective wind speed acting on the rotor. The quality of lidar preview can be defined by the following transfer function: (Schlipf, 2015; Simley and Pao, 2013; Guo et al., 2023)

$$|G_{\text{RL}}(f)| = \frac{|S_{\text{RL}}(f)|}{S_{\text{LL}}(f)}, \quad (5)$$

where  $S_{\text{LL}}$  is the auto-spectrum of lidar-estimated REWS and  $S_{\text{RL}}$  is the cross-spectrum between lidar-estimated and rotor-based REWSs. An analytical solution of  $S_{\text{RL}}$  and  $S_{\text{LL}}$  for specific Mann turbulence parameters, turbine rotor size, and lidar trajectory configuration has been derived by, e.g., Mirzaei and Mann (2016); Held and Mann (2019); Guo et al. (2022a, 2023). In practice, a first-order linear low-pass filter is designed to have a cutoff frequency  $f_{\text{cutoff}}$ , which corresponds to the frequency where the transfer function  $|G_{\text{RL}}(f)|$  reaches -3 dB (Schlipf, 2015; Simley et al., 2018). A higher value of  $f_{\text{cutoff}}$  indicates that more frequency components in the lidar-estimated REWS can be used for feedforward pitch control.

Once the cutoff frequency of the low-pass filter is determined, a buffer time  $T_{\text{buffer}}$  can be further determined, which ensures the feedforward pitch command is activated at the proper time. It can be calculated by (Schlipf, 2015; Guo et al., 2023)

$$T_{\text{buffer}} = T_{\text{lead}} - T_{\text{filter}} - T_{\text{pitch}} - \frac{1}{2}T_{\text{lidar}}, \quad (6)$$

where  $T_{\text{lead}}$  is the time required by turbulence fields to propagate the lidar-focused position to the rotor plane (also called leading time),  $T_{\text{pitch}}$  is the time delay of the pitch actuator,  $T_{\text{lidar}}$  is the lidar full-scan time, and  $T_{\text{filter}}$  is the time delay caused by low-pass and notch filtering. For the four-beam lidar considered here,  $T_{\text{lidar}}$  equals 1 s because each beam direction takes 0.25 s to finish measurement.  $T_{\text{lead}}$  can be approximated by  $\Delta x/U_{\text{Ref}}$ , where  $\Delta x$  is the distance between the lidar measured plane and the rotor position, and  $U_{\text{Ref}}$  is the mean wind speed of turbulence convection (usually assumed to be  $U_{\text{hub}}$ ). The time delays of the pitch actuator and filter can both be calculated using the frequency responses of their transfer functions as

$$T_{\text{filter}}(f) = \frac{\theta_{\text{filter}}(f)}{360f} \quad \text{and} \quad T_{\text{pitch}}(f) = \frac{\theta_{\text{pitch}}(f)}{360f}, \quad (7)$$

where  $\theta_{\text{filter}}$  and  $\theta_{\text{pitch}}$  are the lagging phase responses of the filters and pitch actuator transfer functions in degrees, respectively. They are both functions of frequency, and the values at 0.025 Hz are chosen for the IEA 15 MW turbine because this is the critical frequency near where the rotor has higher fluctuations. In the used ROSCO (version 2.6.0), the pitch actuator of the 15 MW turbine is modeled as a second-order system with a natural frequency of 0.25 Hz and a damping ratio of 0.7 (Abbas et al., 2022).

Because Stability 2 in Table 3 has a dominant probability of occurrence, we choose its turbulence parameters and consider the IEA 15 MW turbine rotor with a four-beam pulsed lidar to calculate  $f_{\text{cutoff}}$  under different lidar trajectory configurations. The four lidar beam directions are assumed to have an identical opening angle  $\beta_{\text{oa}}$  with the negative  $x$ -axis direction, and their projections on the  $yz$ -plane have angles of  $45^\circ$ ,  $135^\circ$ ,  $225^\circ$ , and  $315^\circ$  to the positive  $y$  axis, respectively. The optimization variables are the opening angle of the four beams and the focused upstream distance  $\Delta x$ . With the discussion above, the lidar trajectory optimization problem can be formulated as

$$\begin{aligned} & \max_{\beta_{\text{oa}}, \Delta x} f_{\text{cutoff}}, \\ & \text{s.t. } |G_{\text{RL}}(f_{\text{cutoff}})| = -3, \text{ dB} \quad \text{and} \quad T_{\text{buffer}} > 0. \end{aligned} \quad (8)$$

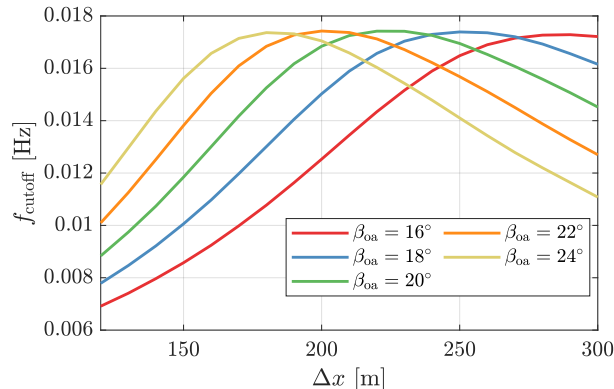


**Figure 5.** The cutoff frequencies of low-pass filters for lidar-assisted control under various lidar measurement trajectories, calculated with a mean wind speed of  $16 \text{ m s}^{-1}$ .

To find an optimal trajectory defined by the opening angle  $\beta_{0a}$  and the focused distance  $\Delta x$ , several discrete configurations are considered. For each above-rated wind speed from 12 m to 24 m, we calculate  $f_{\text{cutoff}}$  and  $T_{\text{buffer}}$ , considering  $\beta_{0a}$  varying from  $16^\circ$  to  $24^\circ$  with a step of  $2^\circ$  and  $\Delta x$  varying from 120 m to 300 m with a step of 10 m. Figure 5 shows the cutoff frequencies of low-pass filters under various lidar measurement trajectories for a mean wind speed of  $16 \text{ m s}^{-1}$ . It can be seen that the maximum cutoff frequency for a smaller opening angle  $\beta_{0a}$  appears at a farther focused distance  $\Delta x$ . The maximum cutoff frequency of different opening angles is generally similar.

In Figure 6, we show the cutoff frequency and buffer time as a function of the mean wind speeds to further help us select the optimal trajectory. Here, we only selected the lidar trajectories that have a peak cutoff frequency in Figure 5. In Figure 6 (a), it can be seen that the cutoff frequencies vary with the mean wind speed linearly, and there are no observable differences for the compared lidar trajectories. However, in Figure 6 (b), there are obvious differences in the buffer time. When the buffer time is negative, it means that the lidar-estimated REWS is too late in time after data processing and filtering, such that it contradicts the feedforward control concept; therefore, trajectories with a negative buffer time at above-rated wind speeds should be avoided in principle. In the end, the trajectory with  $\beta_{0a} = 16^\circ$  and  $\Delta x = 280 \text{ m}$  is chosen as the optimal for our analysis later in this paper.

#### 4 Tuning of controller feedback gains

In this section, we perform aeroelastic simulations with various feedback gains to find the optimized values. The optimal gains bring a lower tower base fore-aft bending load, do not lead to rotor overspeed under extreme turbulence conditions, and do not lead to a significant increase in the load on other turbine components.

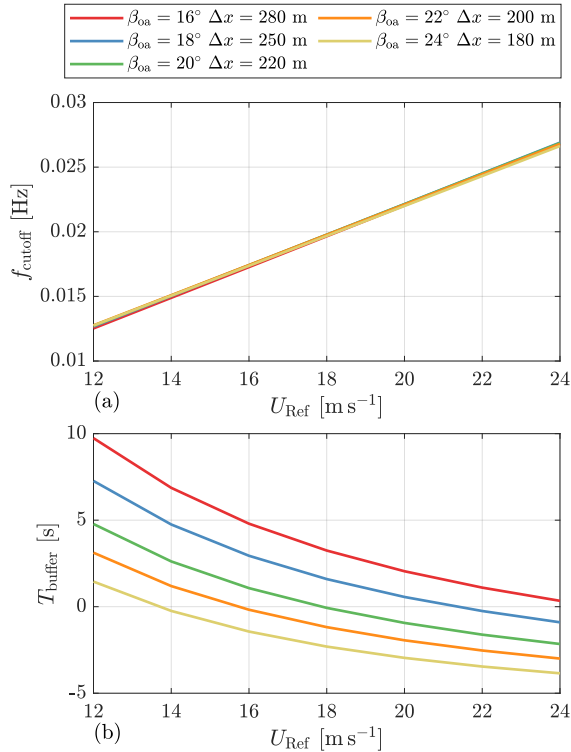


**Figure 6.** The cutoff frequencies and buffer times as a function of the mean wind speeds for several lidar measurement trajectories whose cutoff frequencies are highest (in Figure 5).

#### 4.1 Rotor speed feedback gains

260 To find the optimized gains for the PI controller in the above-rated conditions, we consider the Stability 2 condition with  $U_{\text{hub}}$  values varying from 10 to 24  $\text{m s}^{-1}$  listed in Table 3 and perform simulations with different  $k_p$  and  $T_I$  values. Although the rated wind speed of the IEA 15MW turbine (Gaertner et al.) is 10.59  $\text{m s}^{-1}$ , the  $U_{\text{hub}}=10 \text{ m s}^{-1}$  condition is considered to find the initial gains for gain scheduling. For each mean wind speed condition, the value of  $k_p$  is varied from 0.2 to 1.4 s with a step of 0.2 s and the value of  $T_I$  is varied from 5 to 20 s with a step of 5 s. We have selected the variation ranges of these

265 gains following the studies by Lemmer et al. (2020) and Zalkind et al. (2022). As for the step size selection, we consider the time consumption of simulation and make some compromises. The overall number of simulation cases and, hence, the time required, will rise dramatically if a smaller step size is chosen. However, Figure 7 shows that the step size we chose clearly indicates trends in tower loads. The floating feedback loop gain  $k_{p,\text{float}}$  is considered to be 10 s in these simulations, which will be further optimized in the next section. Also, the feedback gains only depend on the mean wind speed in these simulations.

270 For each mean wind speed with specific  $k_p$  and  $T_I$  values, six independent simulations are performed that have different random seed numbers for generating turbulence and waves. Also, we perform simulations for both design load cases (DLC)

1.2 and 1.3 (IEC 61400-1, 2019). For each DLC with the variations discussed above, there are 1344 simulation cases in total. Each simulation case is executed for 700 s using the periodic turbulence fields and waves, and the initial 100 s results are ignored.

275 For the results of DLC 1.2, we collect the time series and apply the rain flow counting method (Matsuishi and Endo, 1968) to get load amplitudes ( $A_i$ ) and numbers of cycles ( $n_i$ ). After that, the equivalent load amplitude is calculated by

$$A_{\text{eq}} = \left( \sum A_i^m n_i \right)^{\frac{1}{m}}, \quad (9)$$

according to the Palmgren-Miner linear damage hypothesis, where  $m$  is the Wöhler exponent. In this work,  $m = 4$  is considered for the tower and shaft loads,  $m = 10$  is considered for the blade loads, and  $m = 3$  is considered for the mooring chain loads  
 280 (Barrera et al., 2020). The average value of  $A_{\text{eq}}$  by six random seeds is eventually calculated and used as an indication for selecting the optimized gains. The definition of  $A_{\text{eq}}$  is that if a stress with an amplitude of  $A_{\text{eq}}$  is applied to the material once, the resulting damage is equivalent to that caused by the stochastic load. As for the results of DLC 1.3, we collect the maximum values over the results of different seeds.

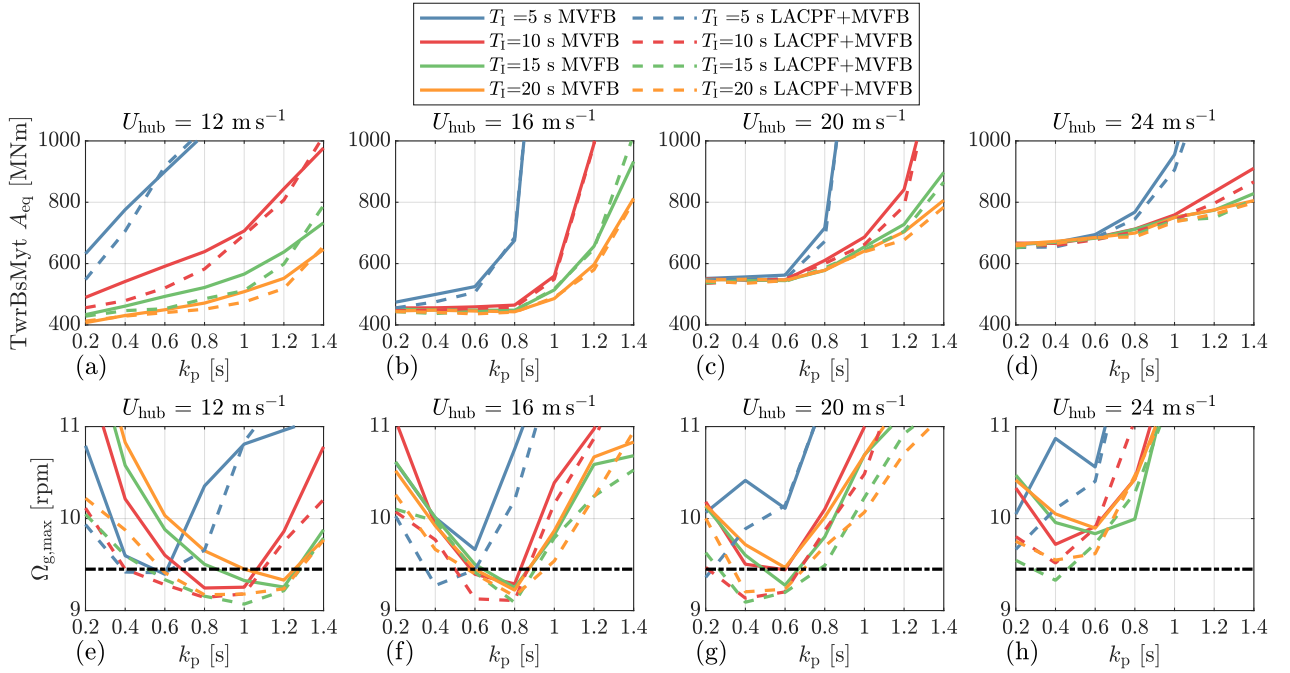


**Figure 7.** Comparisons of equivalent tower base fore-aft bending moment amplitudes and maximum generator speeds under different gains of the PI controller. The dark dashed line indicates an overspeed threshold. Simulated using turbulence spectral parameters from Stability 2. Only parts of the mean wind speed conditions are shown.

Figure 7 shows the equivalent load amplitudes of tower base fore-aft bending moments ( $T_{\text{wrBsM}}_{\text{yt}}$ ) and maximum generator  
 285 speeds by different PI gains under three mean wind speeds as examples. Here, the dark dashed line indicates an overspeed

threshold, which should be avoided during turbine operation and is chosen to be 125% of the rated generator speed (Zalkind et al., 2022). In general, a higher  $k_p$  results in higher tower load amplitudes because the proportional controller is more aggressive regulating the rotor speed by adjusting blade pitch angles; therefore, the rotor thrust force varies more. For a lower mean wind speed, a larger  $k_p$  is required to avoid rotor speed exceeding the 125% threshold, which is similar to the observations by Zalkind et al. (2022). A smaller integral time constant also results in higher loads since the integral controller is more sensitive under the same proportional gain. It would be preferred to use a larger  $T_I$  for load reduction.

Comparing the solid and dashed lines, using LACPF control leads to lower load amplitudes and maximum generator speeds than MVFB control. With MVFB control, it is observed that none of the gains satisfy the rotor speed maximum limit for a very high mean wind speed of  $24 \text{ m s}^{-1}$ . While, when  $k_p = 0.4 \text{ s}$  and  $T_I = 15 \text{ s}$ , introducing LACPF control limits the maximum generator speed within the selected threshold.

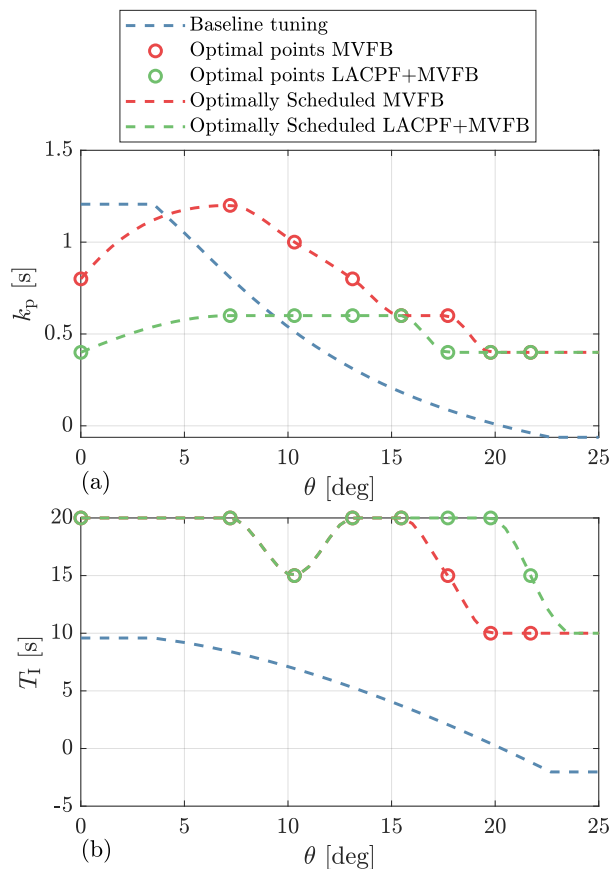


**Figure 8.** The selected optimal gains and the gain scheduling curve for the PI controller. The baseline tuning is provided by the ROSCO toolbox.

Overall, we select the gains according to the following criteria: a) the maximum rotor speed is smaller than the threshold, and b) the gains result in the smallest load amplitude, and they satisfy a). In the case of MVFB control, where a) can not be



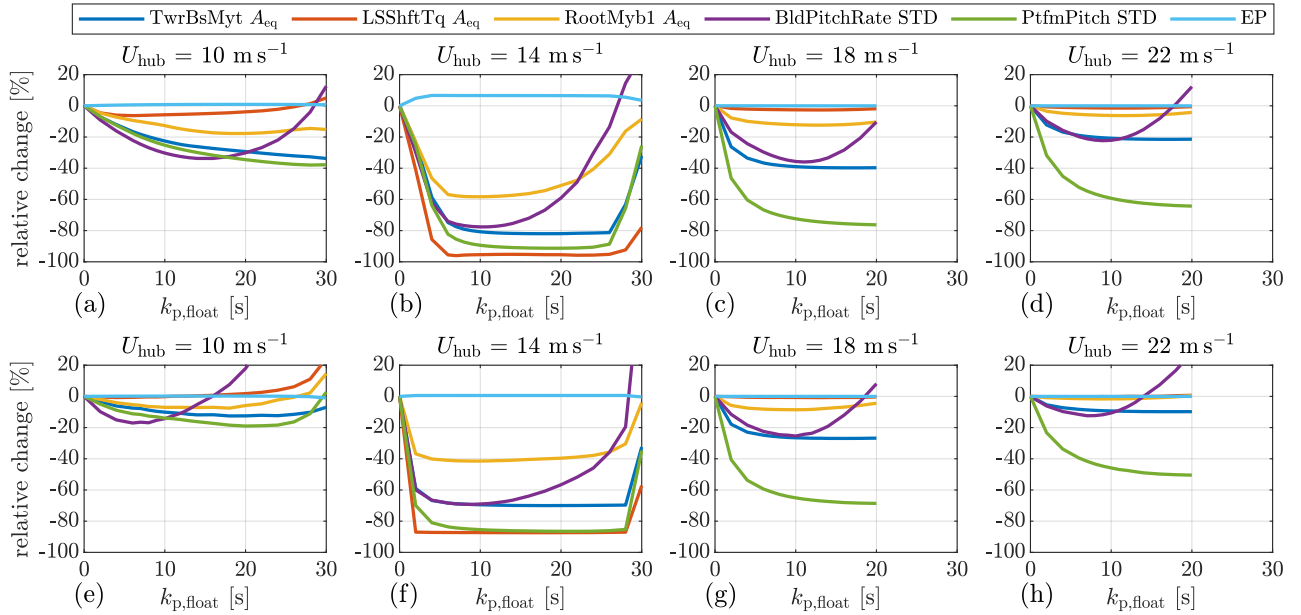


**Figure 9.** Relative changes of equivalent load amplitudes, standard deviations, and energy production under different gains of the platform feedback loop relative to the case  $k_{p,\text{float}} = 0$  s, simulated using turbulence spectral parameters from Stability 2. Only part of the mean wind speed conditions are shown. (a) to (d): MVFB control using optimal PI controller tuning. (e) to (h): LACPF+MVFB control using optimal PI controller tuning.

satisfied, the gains that result in the smallest maximum rotor speed are selected. Figure 8 shows the selected optimal gains, the corresponding scheduled gains by interpolation, and the baseline gain scheduling provided by the ROSCO tool box<sup>4</sup> (Abbas et al., 2022) developed by NREL. Note that the blade pitch angle is used for gain scheduling instead of the mean wind speed. The steady-state blade pitch curve is used for conversion from the mean wind speed to pitch angle. The baseline gain scheduling will be compared with the optimal gain scheduling in Section 5. With LACPF control, it is clear that the PI controller can be less aggressive, especially in small blade pitch angle ranges (the range slightly above the rated wind speed).

## 4.2 Platform feedback gain

In this section, the floating platform pitch feedback gain is further optimized.

We perform simulations for DLC 1.2 using the PI gains obtained from Section 4.1, with  $k_{p,\text{float}}$  ranging from 0 to 30 s or 20 s with a step of 2 s. The  $k_{p,\text{float}}$  values above 20 s are not considered for very high mean wind speeds because they result in a significantly high blade pitch rate. Here, only the DLC cases with a mean wind speed above  $10 \text{ m s}^{-1}$  are considered. The  $A_{\text{eq}}$ , standard deviation (STD), and energy production (EP) are calculated and then compared. Similar to the calculation of  $A_{\text{eq}}$ , the average value of standard deviations and energy productions by six random seeds is computed.

<sup>4</sup><https://github.com/NREL/ROSCO>

**Table 4.** The baseline and optimal (MVFB and LACFF+MVFB) floating platform feedback gains  $k_{p, \text{float}}$  for three control configurations.

$U_{\text{hub}} [\text{m s}^{-1}]$	4	6	8	10	12	14	16	18	20	22	24
Baseline	0	0	0	9.25	9.25	9.25	9.25	9.25	9.25	9.25	9.25
MVFB	0	0	0	24	20	12	12	10	10	10	10
LACFF+MVFB	0	0	0	10	10	10	10	10	10	10	10

To clearly show the control performances of different  $k_{p, \text{float}}$  values, we calculate the relative change from the case  $k_{p, \text{float}} = 0$  s, which means no floating feedback is considered. The considered variables are some of the most important ones for a floating turbine, i.e., the tower base fore-aft bending moment, the low-speed shaft torque (LSShftTq), the blade 1 root out-of-plane bending moment (RootMyb1), the collective blade pitch velocity (BldPitchRate), and the platform fore-aft pitch motion (PfmPitch).  
 315 The blade pitch rate is considered because it is related to the damage to the blade pitch gear and bearing (Guo et al., 2023).

Panels (a) to (d) show the results simulated using MVFB control with optimal PI controller tuning. In general, the STDs of blade pitch rates show parabolic patterns. At the bottom of the parabolic, the blade pitch rate is minimal, meaning a best reduction in the blade pitch activities. As  $k_{p, \text{float}}$  increase, the tower load and platform motion generally tend to be lower (except for the case with a mean wind speed of  $14 \text{ m s}^{-1}$ ). However, their gradients become very small for high values of  
 320  $k_{p, \text{float}}$ . As for the blade and shaft loads, there are also valley points at which the  $k_{p, \text{float}}$  values are close to the  $k_{p, \text{float}}$  at the trough of the blade pitch rate. Except for the case with a mean wind speed of  $14 \text{ m s}^{-1}$ , there is negligible dependence of EP on different floating feedback gains.

Panels (e) to (h) show the results simulated using LACPF+MVFB control with optimal PI controller tuning. In general, the relative changes show a similar trend to that simulated using MVFB control. For a mean wind speed equal to  $10 \text{ m s}^{-1}$ , the  
 325 main difference is that the trough of the blade pitch rate appears at a smaller  $k_{p, \text{float}}$  value in LACPF+MVFB control than in MVFB control.

For both MVFB and LACPF+MVFB controls, at a mean wind speed of  $14 \text{ m s}^{-1}$ , it can be observed that the reductions in all variables are especially significant if the floating feedback gain is considered. The floating feedback loop, in particular, increases the EP in the MVFB control scenario. These are caused by the fact that at this mean wind speed, instability occurs  
 330 if  $k_{p, \text{float}} = 0$  s. For this special case, some examples of time series from one of the six random simulations are provided in Appendix A.

Therefore, based on the discussions above, it is preferable to select  $k_{p, \text{float}}$  where all the structural loads and the blade pitch rates are small. The corresponding  $k_{p, \text{float}}$  values fulfilling the criteria above are those close to the trough of the blade pitch rate. Although a very high  $k_{p, \text{float}}$  helps reduce the platform pitch further, this is undesirable because the structure loads can  
 335 either be higher or reduced marginally while the blade pitch rate becomes much higher. Table 4 summarizes the optimally selected floating gains that are scheduled as a function of the mean wind speed. In addition, the value provided by the ROSCO toolbox (Abbas et al., 2022) is used for the baseline control configuration.

## 5 Controller assessment

In this section, we assess the performances of the three controllers: a) Baseline MVFB controller with ROSCO tuning, b) MVFB  
340 controller with optimal tuning, and c) LACPF+MVFB controller with optimal tuning. Three different groups of turbulence  
spectral parameters representing realistic offshore turbulence characteristics are considered in the fatigue assessment of DLC  
1.2, as listed in Table 3. The spectral parameters for Stability 2 with a higher probability are considered for maximum value  
evaluations of DLC 1.3.

### 5.1 Performance under different environmental conditions

345 The maximum generator speed, platform pitch, platform surge, and blade tip out-of-plane deflection simulated by the three  
control configurations are shown in Figure 10. Compared with the baseline tuning of the MVFB controller, the optimally tuned  
MVFB controller generally has a lower maximum generator speed overshoot. However, the maximum values are above the  
defined threshold (dashed dark line) for most of the above-rated wind speed conditions. The observations here partly contradict  
the optimizations in Figure 7. For example, the generator speed does not exceed the threshold in Figure 7 for a mean wind  
350 speed equal to  $20 \text{ m s}^{-1}$ , but it does in Figure 10. This can be caused by the fact that the PI controller gains are scheduled  
only depending on the mean wind speed in Figure 7, while they are scheduled depending on the blade pitch angle here. It is  
also observed that the optimal PI gains chosen to limit the generator speed have a higher maximum platform pitch and blade  
deflection than the baseline gains at very high wind speeds. As for the maximum surge, the values obtained by optimal tuning  
are slightly lower than those by baseline tuning.

355 Introducing LACPF to MVFB control generally gives the lowest maximum values for all the investigated variables. In  
the case of mean wind speeds equivalent to  $10$  and  $12 \text{ m s}^{-1}$ , the generator speed overshoots are slightly higher than the  
threshold, which should be further improved by more advanced algorithms such as model predictive control (MPC). A MPC  
algorithm utilizes the current state variables and the future wind preview and then calculates the control trajectories by solving  
an optimization problem subjective to certain constraints. The overspeed constraint can, of course, be considered in a lidar-  
360 assisted MPC algorithm (Schlipf et al., 2013; Raach et al., 2014; Lemmer et al., 2015). Except for that, the threshold is not  
exceeded in other wind speed conditions. It is also clear that the maximum values are much lower than those achieved by the  
controllers without the assistance of lidar systems. For very high mean wind speeds, LACPF+MVFB significantly constrains  
the maximum values of platform pitch and blade tip deflection, which are the deficiencies of MVFB optimal tuning control.

Figure 11 shows the relative changes of some important variables by optimally tuned MVFB and LACPF+MVFB controllers  
365 relative to the baseline-tuned MVFB controller. As for stability classes 1 and 3, the simulations are executed excluding the cases  
with mean wind seeds higher than  $12 \text{ m s}^{-1}$  due to their very low probability of occurring. Note that the first fairlead tension  
(FAIRTEN1) is selected for comparison.

Considerable load reductions are achieved in the tower, shaft, and mooring fairlead using the optimally tuned controllers.  
However, a small increment in fairlead tension load is observed for optimally tuned MVFB control. Decrements in platform  
370 pitch and rotor speed are also significant with optimal tuning. On the contrary, the EPs are slightly increased, and the increments

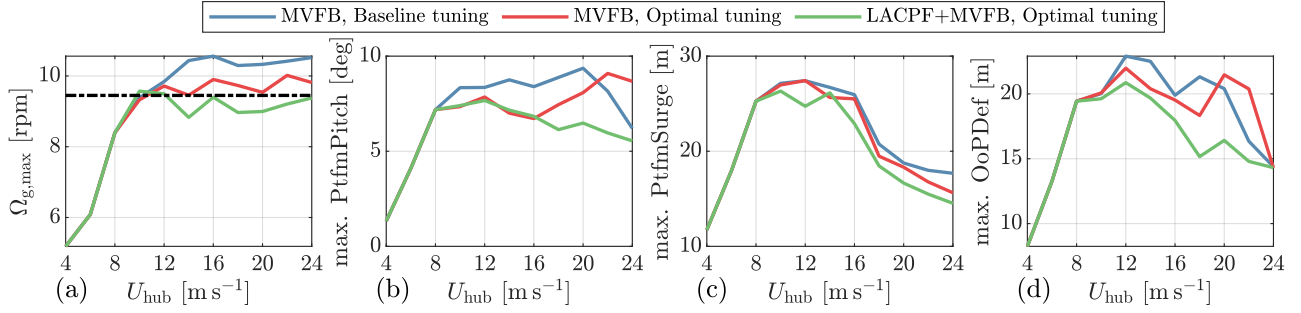


**Figure 10.** Maximum values of some most interested variables for secure operation collected from DLC 1.3, simulated using the turbulence spectra parameters of Stability 2.

are more observable closer to the rated wind speed. In terms of the blade pitch activities, the optimally tuned MVFB controller gives higher blade pitch rates, which are even doubled for very high mean wind speed ranges.

Comparing the performances between optimally tuned LACPF+MVFB and MVFB controls, LACPF+MVFB generally surpasses MVFB controls. More load reductions, higher EP increments, and lower blade pitch consumption are observed in  
 375 LACPF+MVFB control. Although the LACPF control module is designed using the turbulence spectra parameters from Stability 2, these benefits are generally observed in other stability conditions as well. Specially, the tower load by LACPF+MVFB is slightly higher than that by MVFB control in Stability 3, but only at very high wind speeds, where the probability of Stability 3 is much lower than that of Stability 2. Also, using LACPF+MVFB control clearly reduces the blade pitch rate STD close to the rated mean wind speed. In addition, the increment in blade pitch rate by LACPF+MVFB is much lower than those by  
 380 MVFB-only control.

## 5.2 Evaluating lifetime performance

For a more clear indication of the controller's performance, we calculate the lifetime Damage Equivalent Load (DEL) and annual energy production (AEP) by

$$\text{DEL} = \left( \sum_i \sum_j A_{\text{eq},ij}^m \cdot \frac{N_{10\text{min}}}{N_{\text{ref}}} \cdot P_{U_{\text{hub},i}} \cdot P_{\text{sta},j} \right)^{\frac{1}{m}}, \quad (10)$$

385 and

$$\text{AEP} = \sum_i \sum_j EP_{ij} \cdot \frac{N_{10\text{min}}}{20} \cdot P_{U_{\text{hub},i}} \cdot P_{\text{sta},j}. \quad (11)$$

Here,  $i$  and  $j$  are index numbers for mean wind speeds and stability classes. The number  $N_{10\text{min}} = 8765.8 \cdot 6$  is the number of 10 min duration per year and  $N_{\text{ref}}$  is a reference cycle number chosen to be  $2^6$  (Schlipf, 2015). The designed turbine lifetime is considered to be 20 years.

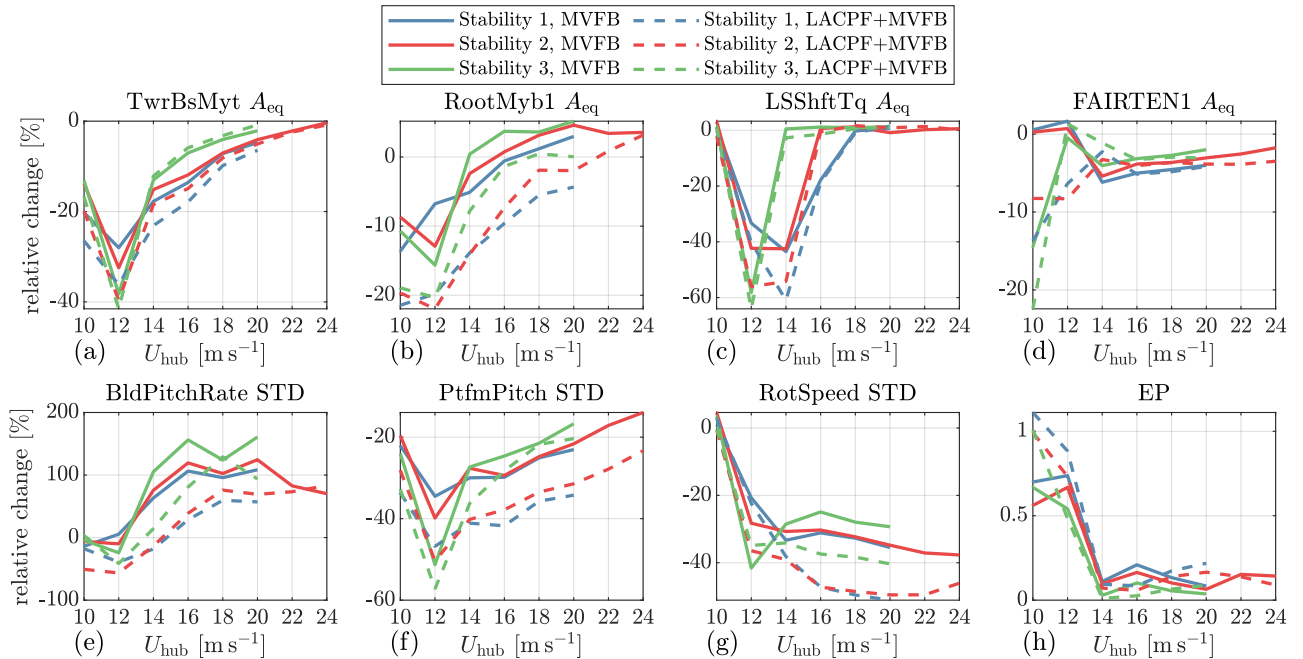


**Figure 11.** Relative changes of equivalent load amplitudes, standard deviations, and energy productions under different mean wind speeds. The relative changes are calculated using the results of optimally tuned MVFB and LACPF+MVFB controllers relative to those of the MVFB controller with baseline tuning.

**Table 5.** The DEL (in MNm unless specified), EL (in years) and AEP (in MWh) by the three control configurations.

Controllers	TwrBsMyt		LSShftTq		RootMyb1		FAIRTEN1		AEP [MWh]	relative change [%]
	DEL	EL	DEL	EL	DEL	EL	DEL [MN]	EL		
MVFB Baseline	409.17		3.79		53.80		1.14		63708.09	
MVFB Opt. tuned	345.89	19.16	3.78	0.29	54.63	-2.85	1.12	0.63	63874.86	0.26
LACPF+MVFB Opt. tuned	335.49	24.25	3.73	1.43	53.15	2.58	1.07	4.15	63915.17	0.33

390 When comparing different DELs, it is convenient to use the extended lifetime (EL)

$$EL = 20 \left( \left( \frac{DEL_i}{DEL_j} \right)^{-m} - 1 \right), \quad (12)$$

where  $i$  and  $j$  are the indexes of different controllers. Here, we have used a definition slightly different from the existing literature, e.g., the study by Simley et al. (2020). In the work by Simley et al. (2020), the term  $\left( \frac{DEL_i}{DEL_j} \right)^{-m}$ , which is the ratio of lifetimes between two controllers, is considered to quantify the benefits of LAC.

395 Table 5 summarizes the DEL, EL, and AEP of the three controllers. Note that the EL and relative change are all calculated relative to the baseline MVFB control. In comparison with the baseline controller, with the optimally tuned MVFB controller,

the DEL of the tower is obviously reduced, leading to an extended lifetime of 19.2 years. Besides, the loads on the shaft and fairlead are slightly reduced. However, the blade root load is clearly increased; therefore, the lifetime is reduced by about 2.9 years. In terms of the AEP, there is a slight increment of about 0.26%. Introducing feedforward control supported by  
400 lidar further improves the overall control performance. With LACPF+MVFB control, the further reduction in tower base load corresponds to a lifetime extension of 5.1 years. Also, the shaft and blade root loads are slightly reduced. As a consequence, the negative impact of optimally tuned MVFB control on blade root load is avoided. The AEP increment under LACPF+MVFB control is also slightly higher than that under MVFB-only control. Further, there is a clear load reduction on the fairlead of the mooring system using LACPF control.

## 405 **6 Conclusions**

This paper assesses lidar-assisted collective pitch feedforward (LACPF) and multi-variable feedback (MVFB) controls for the IEA 15.0 MW reference turbine. The main contributions of this work include: (a) optimization of a four-beam pulsed lidar for controlling a large floating turbine; (b) optimal tuning of speed regulation gains and platform feedback gains for the MVFB, and LACPF+MVFB controllers; and (c) assessing the benefits of the two control strategies using realistic offshore turbulence  
410 spectral characteristics.

The IEC 61400-3 (2009) standard for offshore turbine design does not specify turbulence spectral parameters for offshore conditions. The typical parameter listed in IEC 61400-1 (2019) tends to underestimate the occurrence of large-scale coherent turbulent eddies. In the time domain, these eddies are reflected as low-frequency and spatially correlated turbulence. We have defined realistic turbulence parameters representative of an offshore site based on literature, which are further used for load  
415 and extreme value assessments.

A four-beam, single-range pulsed lidar is optimized for control. For the large rotor floating turbine, it is found that a lidar focusing at a further distance can better estimate the rotor-effective wind speed. A notch filter is necessary for floating turbines to avoid LACPF conflicting with MVFB. Because of the notch filter, additional time delays are introduced by the filtering. A further focusing distance for the lidar system helps to avoid the LACPF command reacting too late.

The speed-regulating proportional-integral controllers are re-tuned, aiming to minimize the tower loads and avoid overspeed. When tuning with LACPF, the optimal values for the proportional gains are found to be lower than those tuned without LACPF. In very high wind speed ranges, the tuning results with or without LACPF are similar. The optimal integral time constants are found to be generally similar, whether considering LACPF or not. The floating feedback gains are also optimized. The optimal values are found to be close to the valley where the blade pitch rates are the lowest. After the valley, increasing the floating  
425 feedback gains has marginal reductions in tower load but amplifies the blade pitch actions significantly.

The control performances of the optimally tuned controllers are assessed and compared to those of a baseline controller provided by NREL's Reference OpenSource Controller toolbox. It is observed that the re-tuning of the gains clearly reduces the maximum generator speed. While there are still some overshoots of generator speed higher than the selected threshold (125 %of rated speed). The overspeed is minimal using LACPF control and is slightly higher than the threshold, which should

430 be further improved in future work. Significant reductions in the maximum values of blade tip deflection and platform pitch are observed using LACPF+MVFB control. In terms of the fatigue load, the most significant improvement from re-tuning the feedback loops with MVFB control is the extension of the tower lifetimes by 19.2 years. If a lidar system is deployed, the tower lifetime can be extended by 24.3 years, and the fairlead lifetime can be 4.2 years longer. There are also extensions of shaft and blade lifetimes of 1.4 and 2.6 years, respectively.

435 For both MVFB and LACPF+MVFB controls, there is clearly an increase in blade pitch activities at very high wind speeds, which can potentially cause more damage to the gear and bearing of the pitch actuator. For the LACPF+MVFB control, there are decrements in the pitch activities close to the rated wind speed. Because the mean wind speed has a higher probability here, it could be possible that the LACPF+MVFB control overall does not cause more damage to the pitch actuator. However, a more detailed assessment can be further improved by more complicated modeling of the pitch actuator damage.

440 Also, the fatigue analysis of the mooring system can be further extended. The potential of LACPF to reduce the load on mooring systems can be further explored by other feedforward control strategies.

*Code availability.* The OpenFASTv3.0 version with a lidar simulator integrated, the 4D Mann turbulence generator, and the source code of a reference lidar-assisted controller are all available from the repository: <https://github.com/MSCA-LIKE>.

445 *Author contributions.* FG conceived the concept, performed the simulations and prepared the manuscript. DS supported to verify the simulation results, contributed in editing, and provided general guidance.

*Competing interests.* The authors declare that they have no conflict of interest.

*Acknowledgements.* This research received financial supports from the European Union's Horizon 2020 research and innovation program under the Marie Skłodowska-Curie grant agreement No. 858358 (LIKE – Lidar Knowledge Europe).

## Appendix A

450 An example time series of the OpenFAST simulations is shown in Figure A1. For the three control configurations, the results are simulated using the turbulence fields generated by the identical random seed. Panel (a) shows the raw line-of-sight measurement provided by the “LidarSim” module. The measurements are performed at different beam directions; therefore, there are considerable high-frequency fluctuations caused by the uncorrelated high-frequency components in the turbulence field. The missing and unconnected points are unavailable line-of-sight measurements due to blade blockage. Panel (b) shows the  
455 lidar estimated and filtered REWS, which is the coherent low-frequency component in the turbulence.

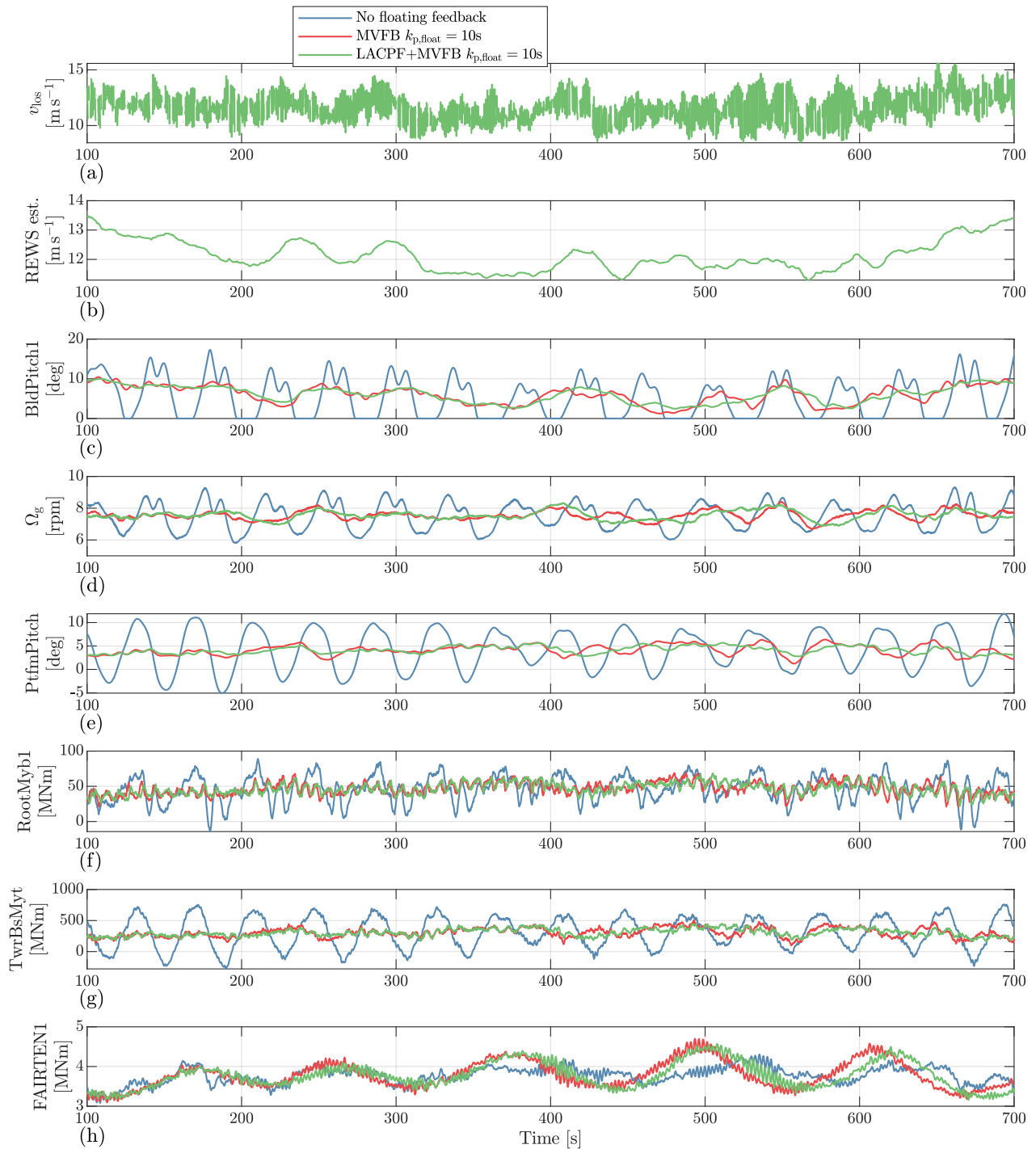


**Figure A1.** Example time series of the OpenFAST simulations, simulated with a mean wind speed of  $12 m s^{-1}$ .



## References

- Abbas, N. J., Zalkind, D. S., Pao, L., and Wright, A.: A reference open-source controller for fixed and floating offshore wind turbines, *Wind Energy Science*, 7, 53–73, <https://doi.org/10.5194/wes-7-53-2022>, 2022.
- Allen, C., Viscelli, A., Dagher, H., Goupee, A., Gaertner, E., Abbas, N., Hall, M., and Barter, G.: Definition of the UMaine VoltturnUS-S  
460 Reference Platform Developed for the IEA Wind 15-Megawatt Offshore Reference Wind Turbine, Tech. Rep. NREL/TP-5000-76773, NREL, <https://doi.org/10.2172/1660012>, 2020.
- Bachynski, E. E. and Eliassen, L.: The effects of coherent structures on the global response of floating offshore wind turbines, *Wind Energy*, 22, 219–238, <https://doi.org/https://doi.org/10.1002/we.2280>, 2019.
- Barrera, C., Battistella, T., Guanche, R., and Losada, I. J.: Mooring system fatigue analysis of a floating offshore wind turbine, *Ocean  
465 Engineering*, 195, 106670, <https://doi.org/https://doi.org/10.1016/j.oceaneng.2019.106670>, 2020.
- Bossanyi, E. A., Kumar, A., and Hugues-Salas, O.: Wind turbine control applications of turbine-mounted LIDAR, *Journal of Physics: Conference Series*, 555, 012011, <https://doi.org/10.1088/1742-6596/555/1/012011>, 2014.
- Bredmose, H., Lemmer, F., Borg, M., Pegalajar-Jurado, A., Mikkelsen, R., Larsen, T. S., Fjelstrup, T., Yu, W., Lomholt, A., Boehm, L., and  
470 Armendariz, J. A.: The Triple Spar campaign: Model tests of a 10MW floating wind turbine with waves, wind and pitch control, *Energy Procedia*, 137, 58–76, <https://doi.org/https://doi.org/10.1016/j.egypro.2017.10.334>, 14th Deep Sea Offshore Wind R&D Conference, EERA DeepWind 2017, 2017.
- CATAPULT, O.: Floating Offshore Wind: Cost Reduction Pathways to Subsidy Free, Tech. rep., CATAPULT, Offshore Renewable Energy, <https://ore.catapult.org.uk>, 2021.
- Cheyne, E., Jakobsen, J. B., and Obhrai, C.: Spectral characteristics of surface-layer turbulence in the North Sea, *Energy Procedia*, 137,  
475 414–427, <https://doi.org/10.1016/j.egypro.2017.10.366>, 14th Deep Sea Offshore Wind R&D Conference, EERA DeepWind'2017, 2017.
- Cheyne, E., Jakobsen, J. B., and Reuder, J.: Velocity spectra and coherence estimates in the marine atmospheric boundary layer, *Boundary-layer meteorology*, 169, 429–460, <https://doi.org/10.1007/s10546-018-0382-2>, 2018.
- de Maré, M. and Mann, J.: Validation of the Mann spectral tensor for offshore wind conditions at different atmospheric stabilities, *Journal of  
Physics: Conference Series*, 524, 012106, <https://doi.org/10.1088/1742-6596/524/1/012106>, 2014.
- 480 DNV-GL: Bladed theory manual: version 4.8, Tech. rep., Garrad Hassan & Partners Ltd., Bristol, UK, 2016.
- Fleming, P. A., Peiffer, A., and Schlipf, D.: Wind turbine controller to mitigate structural loads on a floating wind turbine platform, *Journal of Offshore Mechanics and Arctic Engineering*, 141, <https://doi.org/10.1115/1.4042938>, 2019.
- Gaertner, E., Rinker, J., Sethuraman, L., Zahle, F., Anderson, B., Barter, G. E., Abbas, N. J., Meng, F., Bortolotti, P., Skrzypinski, W.,  
485 Scott, G. N., Feil, R., Bredmose, H., Dykes, K., Shields, M., Allen, C., and Viscelli, A.: IEA Wind TCP Task 37: Definition of the IEA 15-Megawatt Offshore Reference Wind Turbine, <https://doi.org/10.2172/1603478>.
- Guo, F., Mann, J., Peña, A., Schlipf, D., and Cheng, P. W.: The space-time structure of turbulence for lidar-assisted wind turbine control, *Renewable Energy*, <https://doi.org/https://doi.org/10.1016/j.renene.2022.05.133>, 2022a.
- Guo, F., Schlipf, D., Zhu, H., Platt, A., Cheng, P. W., and Thomas, F.: Updates on the OpenFAST Lidar Simulator, *Journal of Physics: Conference Series*, 2265, 042030, <https://doi.org/10.1088/1742-6596/2265/4/042030>, 2022b.
- 490 Guo, F., Schlipf, D., and Cheng, P. W.: Evaluation of lidar-assisted wind turbine control under various turbulence characteristics, *Wind Energy Science*, 8, 149–171, <https://doi.org/10.5194/wes-8-149-2023>, 2023.

- Held, D. P. and Mann, J.: Lidar estimation of rotor-effective wind speed – an experimental comparison, *Wind Energy Science*, 4, 421–438, <https://doi.org/10.5194/wes-4-421-2019>, 2019.
- IEC 61400-1: Wind energy generation systems - Part 1: Design requirements, 2019.
- 495 IEC 61400-3: Wind turbines - Part 3: Design requirements for offshore wind turbines, 2009.
- Jonkman, J.: Influence of Control on the Pitch Damping of a Floating Wind Turbine, <https://doi.org/10.2514/6.2008-1306>, 2008.
- Knight, J. M. and Obhrai, C.: The influence of an unstable turbulent wind spectrum on the loads and motions on floating Offshore Wind Turbines, *IOP Conference Series: Materials Science and Engineering*, 700, 012 005, <https://doi.org/10.1088/1757-899X/700/1/012005>, 2019.
- 500 Lemmer, F.: Low-order modeling, controller design and optimization of floating offshore wind turbines, 2018.
- Lemmer, F., Raach, S., Schlipf, D., and Cheng, P. W.: Prospects of linear model predictive control on a 10MW floating wind turbine, in: *Proceedings of the ASME 34th International Conference on Ocean, Offshore and Arctic Engineering*, St. John's, Canada, <https://doi.org/10.1115/OMAE2015-42267>, 2015.
- Lemmer, F., Müller, K., Yu, W., Schlipf, D., and Cheng, P. W.: Optimization of floating offshore wind turbine platforms with a self-tuning controller, in: *International Conference on Ocean, Offshore and Arctic Engineering*, Trondheim, Norway, <https://doi.org/10.1115/omae2017-62038>, 2017.
- 505 Lemmer, F., Yu, W., Schlipf, D., and Cheng, P. W.: Robust gain scheduling baseline controller for floating offshore wind turbines, *Wind Energy*, 23, 17–30, <https://doi.org/10.1002/we.2408>, 2020.
- Li, L., Gao, Z., and Moan, T.: Joint environmental data at five european offshore sites for design of combined wind and wave energy devices, in: *International Conference on Offshore Mechanics and Arctic Engineering*, vol. 55423, p. V008T09A006, American Society of Mechanical Engineers, <https://doi.org/10.1115/OMAE2013-10156>, 2013.
- 510 Lio, W. H., Meng, F., and Larsen, G. C.: On LiDAR-assisted wind turbine retrofit control and fatigue load reductions, *Journal of Physics: Conference Series*, 2265, 032 072, <https://doi.org/10.1088/1742-6596/2265/3/032072>, 2022.
- Mann, J.: The spatial structure of neutral atmospheric surface-layer turbulence, *Journal of fluid mechanics*, 273, 141–168, 1994.
- 515 Mann, J.: Wind field simulation, *Probabilistic engineering mechanics*, 13, 269–282, 1998.
- Matsuishi, M. and Endo, T.: *Fatigue of metals subjected to varying stress*, Japan Society of Mechanical Engineers, Fukuoka, Japan, 68, 37–40, 1968.
- Meng, F., Lio, W. H., and Larsen, G. C.: Wind turbine LIDAR-assisted control: Power improvement, wind coherence and loads reduction, *Journal of Physics: Conference Series*, 2265, 022 060, <https://doi.org/10.1088/1742-6596/2265/2/022060>, 2022.
- 520 Mirzaei, M. and Mann, J.: Lidar configurations for wind turbine control, *Journal of Physics: Conference Series*, 753, 032 019, <https://doi.org/10.1088/1742-6596/753/3/032019>, 2016.
- NREL: ROSCO. Version 2.6.0, <https://github.com/NREL/ROSCO>, 2021.
- Nybø, A., Nielsen, F. G., Reuder, J., Churchfield, M. J., and Godvik, M.: Evaluation of different wind fields for the investigation of the dynamic response of offshore wind turbines, *Wind Energy*, 23, 1810–1830, <https://doi.org/https://doi.org/10.1002/we.2518>, 2020.
- 525 Obukhov, A.: Turbulence in an atmosphere with a non-uniform temperature, *Boundary-layer meteorology*, 2, 7–29, <https://doi.org/10.1007/BF00718085>, 1971.
- Peña, A.: Østerild: A natural laboratory for atmospheric turbulence, *Journal of Renewable and Sustainable Energy*, 11, 063 302, <https://doi.org/10.1063/1.5121486>, 2019.

- Putri, R. M., Cheynet, E., Obhrai, C., and Jakobsen, J. B.: Turbulence in a coastal environment: the case of Vindeby, *Wind Energy Science*, 7, 1693–1710, <https://doi.org/10.5194/wes-7-1693-2022>, 2022.
- 530 Raach, S., Schlipf, D., Sandner, F., Matha, D., and Cheng, P. W.: Nonlinear model predictive control of floating wind turbines with individual pitch control, in: American Control Conference, Portland, OR, USA, <https://doi.org/10.1109/acc.2014.6858718>, 2014.
- Rivera-Arreba, I., Wise, A. S., Hermile, M., Chow, F. K., and Bachynski-Polić, E. E.: Effects of atmospheric stability on the structural response of a 12 MW semisubmersible floating wind turbine, *Wind Energy*, 25, 1917–1937, <https://doi.org/https://doi.org/10.1002/we.2775>, 535 2022.
- Sandner, F., Schlipf, D., Matha, D., and Cheng, P. W.: Integrated Optimization of Floating Wind Turbine Systems, vol. Volume 9B: Ocean Renewable Energy of *International Conference on Offshore Mechanics and Arctic Engineering*, <https://doi.org/10.1115/OMAE2014-24244>, v09BT09A030, 2014.
- Schlipf, D.: Lidar-Assisted Control Concepts for Wind Turbines, Ph.D. thesis, University of Stuttgart, <https://doi.org/10.18419/opus-8796>, 540 2015.
- Schlipf, D., Sandner, F., Raach, S., Matha, D., and Cheng, P. W.: Nonlinear model predictive control of floating wind turbines, in: Proceedings of the 23rd International Ocean and Polar Engineering Conference, pp. 440–447, Anchorage, USA, <https://doi.org/10.18419/opus-3908>, 2013.
- Schlipf, D., Simley, E., Lemmer, F., Pao, L., and Cheng, P. W.: Collective pitch feedforward control of floating wind turbines using Lidar, 545 *Journal of Ocean and Wind Energy*, 2, 223–230, <https://doi.org/10.17736/jowe.2015.arr04>, 2015.
- Schlipf, D., Fürst, H., Raach, S., and Haizmann, F.: Systems engineering for lidar-assisted control: a sequential approach, in: *Journal of Physics: Conference Series*, vol. 1102, p. 012014, Hamburg, Germany, <https://doi.org/10.1088/1742-6596/1102/1/012014>, windEurope conference 2018 within the Global Wind Summit, 2018.
- Schlipf, D., Lemmer, F., and Raach, S.: Multi-Variable Feedforward Control for Floating Wind Turbines Using Lidar, in: *International Ocean and Polar Engineering Conference*, <https://doi.org/10.18419/opus-11067>, 2020.
- 550 Simley, E. and Pao, L. Y.: Reducing LIDAR wind speed measurement error with optimal filtering, in: Proceedings of the American Control Conference, Washington, DC, USA, <https://doi.org/10.1109/ACC.2013.6579906>, 2013.
- Simley, E., Fürst, H., Haizmann, F., and Schlipf, D.: Optimizing lidars for wind turbine control applications results from the IEA wind task 32 workshop, *Remote Sensing*, 10, 863, <https://doi.org/10.3390/rs10060863>, 2018.
- 555 Simley, E., Bortolotti, P., Scholbrock, A., Schlipf, D., and Dykes, K.: IEA Wind Task 32 and Task 37: Optimizing Wind Turbines with Lidar-Assisted Control Using Systems Engineering, *Journal of Physics: Conference Series*, 1618, 042029, <https://doi.org/10.1088/1742-6596/1618/4/042029>, 2020.
- Somoano, M., Battistella, T., Rodríguez-Luis, A., Fernández-Ruano, S., and Guanche, R.: Influence of turbulence models on the dynamic response of a semi-submersible floating offshore wind platform, *Ocean Engineering*, 237, 109629, 560 <https://doi.org/https://doi.org/10.1016/j.oceaneng.2021.109629>, 2021.
- Taylor, G. I.: The spectrum of turbulence, *Proceedings of the Royal Society of London. Series A-Mathematical and Physical Sciences*, 164, 476–490, <https://doi.org/10.1098/rspa.1938.0032>, 1938.
- van der Veen, G., Couchman, I., and Bowyer, R.: Control of floating wind turbines, in: Proceedings of the American Control Conference, Montreal, Canada, <https://doi.org/10.1109/ACC.2012.6315120>, 2012.
- 565 Ward, D., Collu, M., and Sumner, J.: Reducing Tower Fatigue through Blade Back Twist and Active Pitch-to-Stall Control Strategy for a Semi-Submersible Floating Offshore Wind Turbine, *Energies*, 12, <https://doi.org/10.3390/en12101897>, 2019.

Wu, J. and Kim, M.-H.: Generic Upscaling Methodology of a Floating Offshore Wind Turbine, *Energies*, 14, <https://doi.org/10.3390/en14248490>, 2021.

Zalkind, D., Abbas, N. J., Jasa, J., Wright, A., and Fleming, P.: Floating wind turbine control optimization, *Journal of Physics: Conference Series*, 2265, 042 021, <https://doi.org/10.1088/1742-6596/2265/4/042021>, 2022.